LiMoO$_3$(IO$_3$), a novel molybdenyl iodate with strong second-order optical nonlinearity

A.H. Reshak [a, b, *], S. Auluck [c, d]

[a] New Technologies — Research Centre, University of West Bohemia, Univerzitni 8, 306 14 Pilsen, Czech Republic
[b] Center of Excellence Geopolymer and Green Technology, School of Material Engineering, University Malaysia Perlis, 01007 Kangar, Perlis, Malaysia
[c] Council of Scientific and Industrial Research — National Physical Laboratory, Dr. K S Krishnan Marg, New Delhi 110012, India
[d] Department of Physics, Indian Institute of Technology, Hauz Khas, New Delhi 110016, India

ABSTRACT

The linear and nonlinear optical susceptibilities of molybdenyl iodate LiMoO$_3$(IO$_3$) have been calculated and compared with the available experimental data. The calculated linear optical properties reveal that there exists a considerable anisotropy thereby favoring an enhanced phase matching conditions necessary for observation of the second harmonic generation (*SHG*) and optical parametric oscillation (*OPO*). It has been found that LiMoO$_3$(IO$_3$) posses positive birefringence and negative uniaxial anisotropy. The molybdenyl iodate with $2D - Mo - O$ sheets capped by IO_3^- group is the main source of the *SHG* due to the electronic transition from the lone-pair electrons of oxygen atoms ($O - 2p$) to $Mo - 4d$ and $I - 5p$ states. Moreover, the presence of the alkali metals can give further strength to the *SHG*. We would like to mention that the dipole moments in MoO_6 octahedra and IO_3^- group arranged in a way which strengthens the *SHG*. Our calculated value of the dominant component of the *SHG* agrees well with the experimental value obtained by Chen's group, which is four times larger than that of the well known *KDP* (KH$_2$PO$_4$). Also we found that it is equal to one half of the experimental value of the well known KTiOPO$_4$ (*KTP*) single crystals. Further, from the obtained *SHG* values of the dominant components we have calculated the microscopic first hyperpolarizability at static limit and at $\lambda = 1064$ nm.

© 2015 Elsevier B.V. All rights reserved.

1. Introduction

The nonlinear optical (*NLO*) materials have been considered as potential candidates due to their numerous applications in nonlinear optics and laser engineering. The borate materials BaB$_2$O$_4$, LiB$_3$O$_5$, CsB$_3$O$_5$, BaBiBO$_4$, Bi$_2$ZnB$_2$O$_7$, CaBiGaB$_2$O$_7$, Bi$_2$CaB$_2$O$_7$, Bi$_2$SrB$_2$O$_7$ and YCa$_4$(BO$_3$)$_3$O are all well-known *NLO* crystals [1–4] which show excellent properties such as short growth period, large effective nonlinear coefficient, high damage threshold, and good mechanical properties. Searching for novel nonlinear optical materials which can present a relatively new class of functional materials with large and extremely fast nonlinearities compared to traditional *NLO* crystals is very challenging. A development in the research of nonlinear optics of novel inorganic and organic semiconducting materials, has

gained great interest for second- and third-order *NLO* applications due to their large optical nonlinearities and their ultrafast, almost purely electronic response [5–16]. These materials offer many possibilities to tailor materials with the desired properties through optimization of the microscopic hyperpolarizabilities (molecular engineering) and the incorporation of molecules in a crystalline lattice (crystal engineering) and polymers. The research on inorganic and organic materials for photonic elements is strongly motivated by the need for the development of high transmission bandwidths and wavelength division multiplexing systems in telecommunication technologies [13–16]. For high speed second-order nonlinear optical applications, such as electro-optics, second-harmonic generation (*SHG*), optical parametric oscillation (*OPO*), and optical rectification, including THz wave generation, a highly asymmetric electronic response of the material to the external electric field is required. It is important to understand the relation between the structure and the main sources of the *NLO* properties. Also it is essential to understand the relation between molecular ordering with noncovalent interactions. This can be obtained from calculating and analyzing

the linear optical properties. The calculation of the linear optical properties involve the energy eigenvalues and electron wavefunctions. These are natural outputs of the band structure calculations. Therefore, the linear optical properties give deep insight into the electronic structure. For *NLO* crystals, it is very well known that a different orientation of chromophores essentially affects the macroscopic *NLO* properties [17,18]. However, the influence of various noncovalent interactions on the microscopic and macroscopic nonlinearities is not understood yet [17]. Understanding and exploitation of noncovalent interactions in molecular crystals are therefore a starting point of our motivation for this work. It has been reported that the $LiMoO_3(IO_3)$ represents a new structure type and the first structurally characterized molybdenyl iodate with $2D - Mo - O$ sheets capped by IO_3^- group which is the main sources for *SHG* [19,20]. Furthermore, Hu and Mao [20] reported that $LiMoO_3(IO_3)$, $RbMoO_3(IO_3)$ and $CsMoO_3(IO_3)$ have the same chemical formula and their structure contains several distorted MoO_6 and IO_3^- groups but $LiMoO_3(IO_3)$ presented the highest *SHG* among $RbMoO_3(IO_3)$ and $CsMoO_3(IO_3)$. Therefore, to investigated the reason beyond the strong *SHG* of $LiMoO_3(IO_3)$, we have addressed ourselves to investigate the linear optical susceptibilities of $LiMoO_3(IO_3)$ which will bring us important insights to understand the electronic origins of the nonlinear optical susceptibilities and the hyperpolarizability by employing first-principles calculations using the full potential linear augmented plane wave plus local orbitals $(FP - LAPW + lo)$ method which has proven to be one of the accurate methods [21−24] for the computation of the electronic structure of solids within density functional theory (DFT).

2. Calculation methodology

The current calculations were performed based on the x-ray crystallographic data reported by Chen's group [15]. The geometrical relaxation was achieved within the generalized gradient approximation $(PBE - GGA)$ [25] using the full potential linear augmented plane wave $(FP - LAPW + lo)$ method as embodied in the *WIEN2k* code [26]. The resulting relaxed geometry was used to calculate the linear and nonlinear optical susceptibilities using $PBE - GGA$ and the recently modified Becke-Johnson potential (mBJ) [27]. The crystal structures of $LiMoO_3(IO_3)$ is presented in Fig. 1. The muffin-tin radii (R_{MT}) of the atoms are chosen in such a way that the spheres did not overlap. The value of R_{MT} is taken to be 1.84 a.u. (I), 1.63 a.u. (Li), 1.71 a.u. (Mo) and 1.55 a.u. for O. To achieve the total energy convergence, the basis functions in the interstitial region (IR) were expanded up to $R_{MT} \times K_{max} = 7.0$ and inside the atomic spheres for the wave function. The maximum value of l was taken as $l_{max} = 10$, while the charge density is Fourier expanded up to $G_{max} = 12$ $(a.u)^{-1}$. Self-consistency is obtained using 300 k points in the irreducible Brillouin zone (IBZ). The self-consistent calculations are converged since the total energy of the system is stable within 0.00001 Ry. The linear optical properties are performed within 1500 k points in the IBZ, while the nonlinear optical properties are performed within 2400 k points in the IBZ.

3. Results and discussion

3.1. Linear optical properties and birefringence

Based on the electronic band structure calculations the imaginary and real parts of the frequency dependent optical dielectric functions were calculated. The calculations of the optical dielectric functions involve the energy eigen-values and
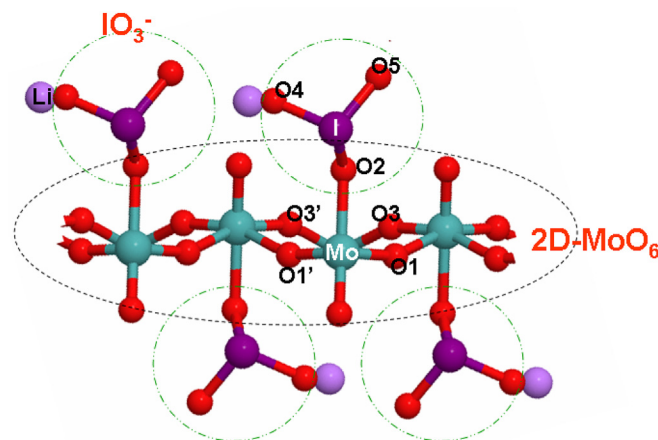

Fig. 1. Crystal structure of $LiMoO_3(IO_3)$. It is clear that the Mo atom occupied a distorted octahedron with short Mo−O6 bond, here O6 is not bound to any other atoms. Four Mo−O−Mo bonds through O1, O1′, O3 and O3′ and one Mo−O−I link by O2. It has been reported that the $LiMoO_3(IO_3)$ represents a new structure type and the first structurally characterized molybdenyl iodate with 2D-Mo-O sheets capped by IO_3^- group.

electron wave-functions. These are natural outputs of band structure calculations, thus the calculated dielectric functions give deep insight to understand the electronic structure. The optical tensors are determined by inter-band transitions between the valence bands (VB) and the conduction bands (CB). According to the dipolar selection rule only transitions changing the angular momentum quantum number l by unity $(\varDelta = \pm 1)$ are allowed. We have calculated $\varepsilon_2^{xx}(\omega)$, $\varepsilon_2^{yy}(\omega)$ and $\varepsilon_2^{zz}(\omega)$, which are the imaginary part of the dielectric function. These completely describe the linear optical response. These tensor components can be obtained from the momentum matrix elements between the occupied and unoccupied wave-functions, giving rise to the selection rules as shown in Fig. 2(a) and (b). To completely identify the origin of the observed optical spectral structures in $\varepsilon_2^{xx}(\omega)$, $\varepsilon_2^{yy}(\omega)$ and $\varepsilon_2^{zz}(\omega)$ we need to carefully look at the magnitude of the optical matrix elements. The observed structures would correspond to those transitions that have large optical matrix elements. To simplify this we have indicated the allowed optical transitions $(\varDelta = \pm 1)$ between the VB and CB using our calculated electronic band structure (Fig. 2(b)). The allowed optical transitions occurs between O-2s/2p, Mo-4p, I-5s/5p/4d, Li-2s and Mo-4p/4d, I-5s/4d, Li-2s states to form the first optical spectral structure. It is interesting to mention that the width of the first optical spectral structure is essentially determined by the width of the highest occupied VB. The second optical spectral structure corresponds to transition between Mo-5s/4p/4d, O-2p, I-5s/5p/4d, Li-2s and Mo-4p/4d, O-2s/2p, Li-2s, I-5s/5p/4d states. The broadening is chosen to be 0.1 eV which is typical of the experimental accuracy and it is traditional for oxide compounds. Since the *mBJ* succeeds by large amount in bringing the calculated energy gap closer to the experimental one (see Fig. S1 − supplementary materials), all discussions are for *mBJ*. The fundamental optical absorption edge for $\varepsilon_2^{xx}(\omega)$, $\varepsilon_2^{yy}(\omega)$ and $\varepsilon_2^{zz}(\omega)$ are located at 2.73 eV, the value of the fundamental optical gap, which confirms the occurrence of the accurate optical transitions between the top of VB and bottom of CB as shown in Fig. 2(b). Following Fig. 2(a) we can see there exists a considerable anisotropy between the optical tensor components in the [100], [010] and [001] polarization directions. This anisotropy favors an enhanced phase matching conditions necessary for observation of *SHG* and *OPO*. It has been noticed

that after the first absorption edges there is rapid increases in the optical absorption to form the first pronounced peak around 4.8 eV, after some oscillations the optical spectral of the three tensor components drop to the lowest values forming a lossless region around 12.5 eV.

The associated real parts of the optical dielectric function in the [100], [010] and [001] polarization directions are obtained from the imaginary part using the Kramers−Kronig transformation [28]. The calculated real parts were presented in Fig. 2(a), again it shows significant anisotropy between the optical tensor components. The vanishing frequency value of the dielectric function defines the static electronic dielectric constant $\varepsilon_1^{xx}(0)$, $\varepsilon_1^{yy}(0)$ and $\varepsilon_1^{zz}(0)$, these values are listed in Table 1. Using Penn model [29] we can obtained the value of the energy band gap from $\varepsilon_1^{xx}(0)$, $\varepsilon_1^{yy}(0)$ and $\varepsilon_1^{zz}(0)$. Penn proposed a relation between $\varepsilon(0)$ and E_g, $\varepsilon(0) \approx 1 + (\hbar\omega_P/E_g)^2$, where E_g is the energy band gap. Therefore, the optical properties help to obtain the value of the energy band gap directly from the imaginary part and indirectly from the real part. There are several other important features in the optical spectrum, such as the uniaxial anisotropy $\delta\varepsilon = [(\varepsilon_0^{II} - \varepsilon_0^{\perp})/\varepsilon_0^{average}]$ which can be calculated using the existence values of the static electronic dielectric constant. Following this formula we find that LiMoO$_3$(IO$_3$) exhibits negative uniaxial anisotropy (Table 1). We would like to highlight the other features in the optical spectrum, these are the plasmon oscillations ω_p^{xx}, ω_p^{yy} and ω_p^{zz}, which are associated with inter-band transitions. The plasmon maximum is usually the most intense feature in the optical spectrum and this is at energy where $\varepsilon_1^{xx}(\omega)$, $\varepsilon_1^{yy}(\omega)$ and $\varepsilon_1^{zz}(\omega)$ crosses zero which is associated with the existence of plasma oscillations. The obtained values of the plasma frequency are presented in Table 1. A deep insight into the electronic structure can further be obtained by calculating the optical conductivity $\sigma(\omega)$, absorption coefficient $I(\omega)$, reflectivity spectra $R(\omega)$, refractive indices $n(\omega)$ and the associated birefringence $\Delta n(\omega)$ and compared with the available experimental data [19].

The optical conductivity consist of imaginary part $\sigma_2(\omega)$ and real part $\sigma_1(\omega)$, each part consist of three tensor components along [100], [010] and [001] polarization directions as shown in Fig. 2(c). The optical conductivity can be calculated using the expression $\varepsilon(\omega) = \varepsilon_1(\omega) + i\varepsilon_2(\omega) = 1 + \frac{4\pi i\sigma(\omega)}{\omega}$, which show that $\sigma(\omega)$ is directly related to the complex dielectric function. Following Fig. 2(c), the imaginary part $\sigma_2^{xx}(\omega)$, $\sigma_2^{yy}(\omega)$ and $\sigma_2^{zz}(\omega)$ between 0.0 and the values of ω_p^{xx}, ω_p^{yy} and ω_p^{zz} exhibit overturned features of $\varepsilon_2^{xx}(\omega)$, $\varepsilon_2^{yy}(\omega)$ and $\varepsilon_2^{zz}(\omega)$, whereas the real parts $\sigma_1^{xx}(\omega)$, $\sigma_1^{yy}(\omega)$ and $\sigma_1^{zz}(\omega)$ show similar features to that of $\varepsilon_2^{xx}(\omega)$, $\varepsilon_2^{yy}(\omega)$ and $\varepsilon_2^{zz}(\omega)$. However, at higher frequencies the spectrum deviates significantly from the prediction of the Drude theory, according to which the optical conductivity should drop down to zero as $1/\omega^2$. Fig. 2(d) illustrates the calculated absorption coefficient $I(\omega)$ along [100], [010] and [001] polarization directions. It shows the fundamental optical absorption edges situated at 2.73 eV thus matching the experimental value of the absorption edges (2.80 eV) [19]. A rapid increase occurs after the absorption edges to reach the maximum absorption at around 10.0 eV. It is clear that LiMoO$_3$(IO$_3$) posses wide optical transparency region up to 2.73 eV ($\lambda = 4542$ Å) in good agreement with the experimental data to 2.80 eV ($\lambda = 4428$ Å) [19]. In Fig. S2 (supplementary materials) we present the calculated $I(\omega)$ in comparison with the experimental data [19], good agreement was found in the matter of the absorption edge.

The calculated optical reflectivity spectra along the polarization directions [100], [010] and [001] are shown in Fig. 2(e). It has been found that the first reflectivity minima occurs at 7.35, 4.73 and 9.70 eV for $R^{xx}(\omega)$, $R^{yy}(\omega)$ and $R^{zz}(\omega)$, respectively. These are the positions where the values of plasma resonance situated which confirms the occurrence of a collective plasmon resonance in concordance with our observation in Fig. 2(a,c,d). The calculated lossless function (Fig. 2(f)) as a function to photon energy exhibits that there exists a lossless region between 12.0 eV and 13.5 eV in concordance with Fig. 2(a,c,d,e).

Fig. 2(g) illustrated the calculated refractive indices for the three polarization directions. The calculated values of the refractive indices at the static limit are listed in Table 1. It has been noticed that $n^{xx}(\omega)$, $n^{yy}(\omega)$ and $n^{zz}(\omega)$ reach their maximum value at 4.2 eV for $n^{xx}(\omega)$ and $n^{zz}(\omega)$ while at 3.8 eV for $n^{yy}(\omega)$, then gradually decreases to go beyond unity. Using the existence values of $n^{xx}(\omega)$, $n^{yy}(\omega)$ and $n^{zz}(\omega)$ the values birefringence $\Delta n(\omega)$ can be obtained at any wavelength as shown in Fig. 2(h). The birefringence is important only in the non-absorbing spectral range, which is below the energy gap. The birefringence is the difference between the extraordinary and ordinary refraction indices, $\Delta n(\omega) = n_e(\omega) - n_o(\omega)$, where $n_o(\omega)$ is the index of refraction for an electric field oriented along the **c**-axis and $n_e(\omega)$ is the index of refraction for an electric field perpendicular to the **c**-axis. The calculated value of the birefringence at zero limit is listed in Table 1. It has been found that LiMoO$_3$(IO$_3$) exhibit a positive birefringence favors an enhanced phase matching conditions necessary for the SHG and OPO.

3.2. Second harmonic generation and hyperpolarizability

LiMoO$_3$(IO$_3$) crystallized in non-centro-symmetry structure monoclinic space group P2$_1$, this symmetry allows eight nonzero complex second-order nonlinear optical susceptibility tensors $\chi_{113}^{(2)}(-2\omega;\omega;\omega)$, $\chi_{123}^{(2)}(-2\omega;\omega;\omega)$, $\chi_{213}^{(2)}(-2\omega;\omega;\omega)$, $\chi_{223}^{(2)}(-2\omega;\omega;\omega)$, $\chi_{311}^{(2)}(-2\omega;\omega;\omega)$ $\chi_{312}^{(2)}(-2\omega;\omega;\omega)$, $\chi_{322}^{(2)}(-2\omega;\omega;\omega)$ and $\chi_{333}^{(2)}(-2\omega;\omega;\omega)$. The complex second-order nonlinear optical susceptibility tensor formulas are given elsewhere [30−33].

In Fig. 3(a) the absolute value $\left|\chi_{ijk}^{(2)}(\omega)\right|$ of the eight tensors components were illustrated, It has been found that $\left|\chi_{223}^{(2)}(\omega)\right|$ exhibits the highest value among the other tensors components at the static limit. Therefore, $\left|\chi_{223}^{(2)}(\omega)\right|$ is the dominant component at the static limit, while $\left|\chi_{333}^{(2)}(\omega)\right|$ is the dominant component at the wavelength 1064 nm. The values of $\left|\chi_{ijk}^{(2)}(\omega)\right|$ for all tensors components at static limit and at wavelength 1064 nm were evaluated and presented in Table 2 along with the well-know nonlinear optical crystals for seeking a meaningful comparison. We would like to mention that, knowing the static values of the second order susceptibility tensor are essential to estimate their relative SHG efficiency. From Table 2 we find that our calculated value of SHG for the dominant component is agree well with the experimental value obtained by Chen et al. [19] which was four times larger than that of the well-know NLO crystal KDP (KH$_2$PO$_4$). Also it is one half of the experimental value of the well known KTiOPO$_4$ (KTP) single crystals which exhibits a SHG value of about 16.9 [34], 13.7 [35], 15.4 ± 0.2 [36], 14.6 ± 1.0 [37], 17.4 ± 1.7 [38], 16.9 ± 3.3 [39], 16.9 ± 1.7 [40], 10.6 ± 7.5 [41], 16.75 [42] and 16.65 [42] at $\lambda = 1064$ nm.

We should emphasize that LiMoO$_3$(IO$_3$) is characterized by the combination of distorted MoO$_6$ octahedron and IO$_3^-$ group [44,45]. Each MoO$_6$ is sharing their corners with the neighboring octahedron to form 2D molybdenum oxide sheets,
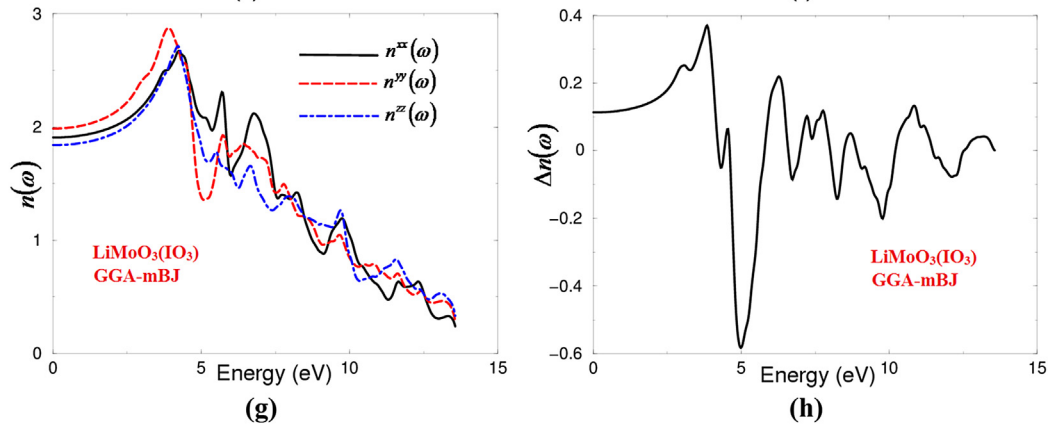
(a)

(b)

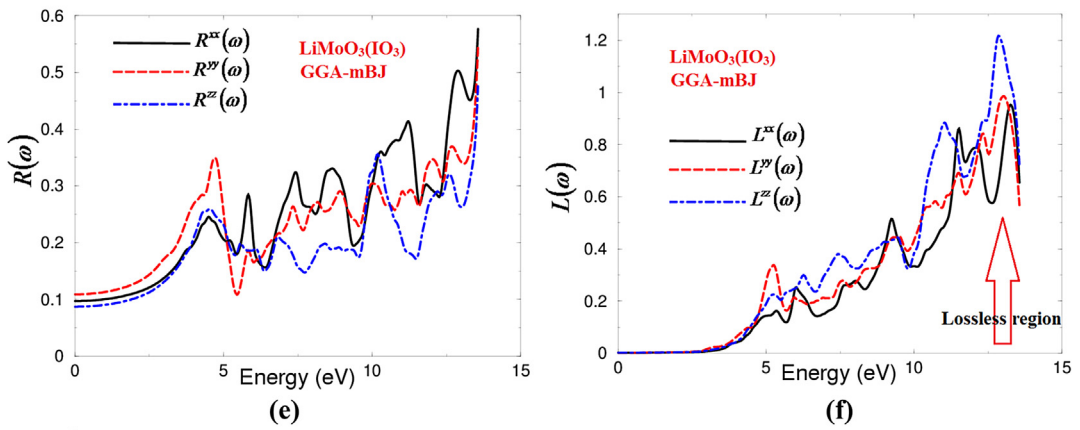(c)

(d)

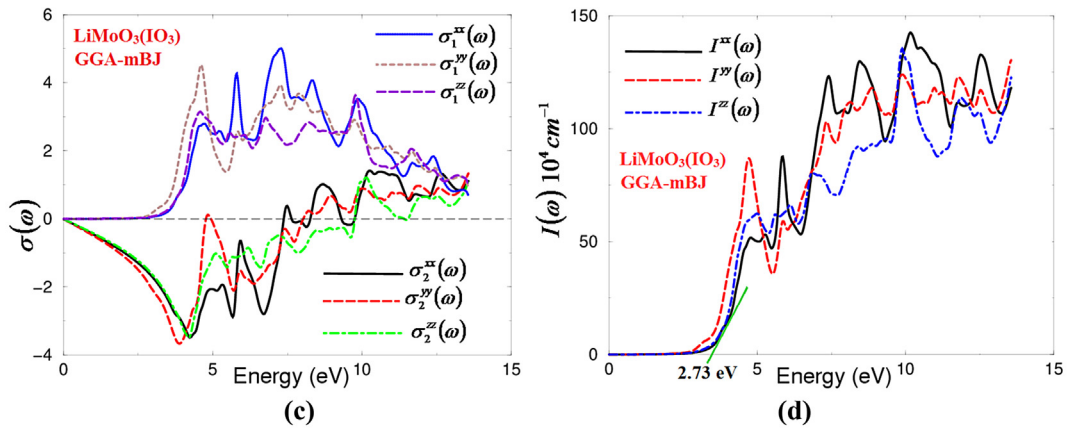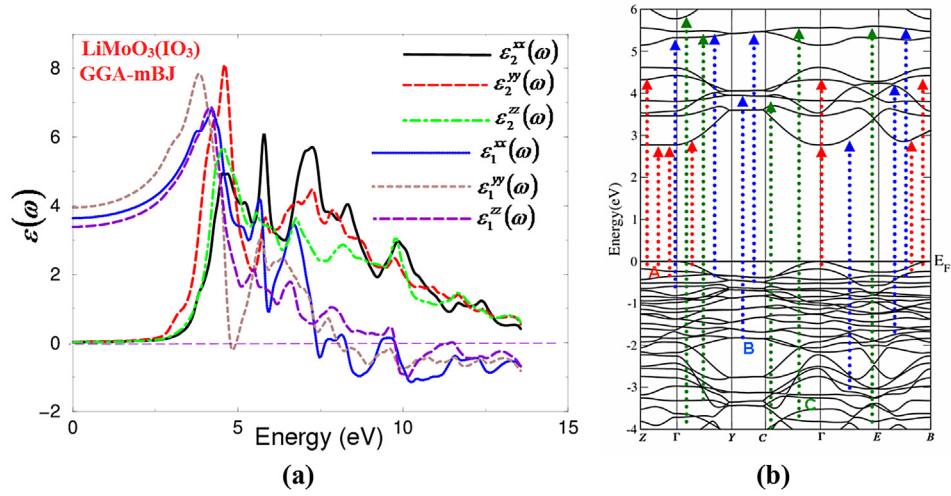(e)

(f)

(g)

(h)

Table 1
The calculated energy band gap in comparison with the experimental value, $\varepsilon_1^{xx}(0)$, $\varepsilon_1^{yy}(0)$, $\varepsilon_1^{zz}(0)$, $\varepsilon_1^{average}(0)$, $\delta\varepsilon$, ω_p^{xx}, ω_p^{yy}, ω_p^{zz}, $n^{xx}(0)$, $n^{yy}(0)$, $n^{zz}(0)$ and $\Delta n(0)$.

Parameters	Values using PBE-GGA	Values using mBJ
Eg (eV)	2.15	2.73, **2.80**[a] **(exp.)**
$\varepsilon_1^{xx}(0)$	4.74	3.63
$\varepsilon_1^{yy}(0)$	5.11	3.94
$\varepsilon_1^{zz}(0)$	4.37	3.38
$\varepsilon_1^{average}(0)$	4.74	3.65
$\delta\varepsilon$	−0.11	−0.12
ω_p^{xx}	9.15	7.38
ω_p^{yy}	9.04	8.04
ω_p^{zz}	9.15	9.78
$n^{xx}(0)$	2.17	1.90
$n^{yy}(0)$	2.26	1.98
$n^{zz}(0)$	2.09	1.83
$\Delta n(0)$	0.13	0.11

[a] Ref. [19] (experimental value).

thus $LiMoO_3(IO_3)$ exhibits a new structure type that is attributed to the fact that the molybdenyl iodate with $2D − Mo − O$ sheets capped by IO_3^- group [19]. This is the main source of the *SHG* due to the electronic transition from the lone-pair electrons of oxygen atoms (O-2p) to Mo-4d and I-5p states. Moreover, there is another source to the *SHG* which is due to the presence of the alkali metals [20]. We would like to mention that the arrangement of the dipole moments in MoO_6 octahedra and IO_3^- group favors a strong *SHG* [19]. That is attributed to the fact that the *SHG* response in the non-centro-symmetric materials is due to the anionic group according to Chen's anionic group theory [46]. Since the energy band gap comes in the denominator of the complex second-order nonlinear optical susceptibility tensor formulas which turn the *SHG* to be very sensitive to the band gap value [43,47]. Therefore, we have used the recently modified Becke-Johnson potential to overcome the underestimation of the band gap cause by *DFT* calculations. It is a consequence of a fact that the *DFT* calculations usually underestimate the energy gaps with respect to the experimental values. A very simple way to overcome this drawback is to use the scissors correction, which merely brings the calculated energy gap close to the experimental gap. The scissors correction is the difference between the calculated and measured energy gaps. Although the *mBJ* succeeds by large amount in bringing the calculated energy gap closer to the experimental one, we have applied the scissors correction to bring the value of the calculated energy gap to be exactly as the measured one. Furthermore, we have calculated the imaginary and real parts of the eight tensors components but we will present only the results of the dominant component $\chi_{223}^{(2)}(-2\omega; \omega; \omega)$ as shown in Fig. 3(b). The figure show that the imaginary part has zero value below the half value of the fundamental energy gap then starts rising at the half value of the gap due to the appearance of the 2ω resonance. Above the

fundamental energy gap the ω resonance begins to contribute in addition to 2ω and give the major contribution to the *SHG*, while in the high energy region the contribution comes from ω resonance only. To explain this we have plotted the $2\omega/\omega$ inter-/intra-band contributions to the total $Im\chi_{223}^{(2)}(\omega)$ (dominant component). It is clear that each of ω and 2ω resonances can be further separated into inter-band and intra-band contributions as shown in Fig. 3(c). Further explanation can be obtained the comparison of $\left|\chi_{223}^{(2)}(\omega)\right|$ with the absorptive part of the corresponding dielectric function $\varepsilon_2(\omega)$ as a function of both $\omega/2$ and ω as shown in Fig. 3(d). We can divide the spectral structure of $\left|\chi_{223}^{(2)}(\omega)\right|$, $\varepsilon_2(\omega)$ and $\varepsilon_2(\omega/2)$ into three regions. The first region (1.4 eV−2.80 eV) is mainly originated from 2ω resonance, the second region (2.80 eV−7.0 eV) is associated with interference between 2ω and ω resonances. The third region (7.0 eV−14.0 eV) is mainly due to ω resonance.

For more information regarding the $LiMoO_3(IO_3)$, the microscopic first hyperpolarizability, β_{ijk}, the vector components along the dipole moment direction was calculated at static limit and at $\lambda = 1064$ nm (1.165 eV), using β_{ijk} expression which is given elsewhere [48]. The microscopic first hyperpolarizability terms cumulatively yield a bulk observable second order susceptibility term, $\chi_{ijk}^{(2)}(\omega)$, which in turn is responsible for the high *SHG* response [49,50]. These values are listed in Table 2.

4. Conclusions

Based on the calculated electronic band structure using the full potential linear augmented plane wave within the recently modified Becke-Johnson potential (*mBJ*) potential, we have calculated the linear and nonlinear optical susceptibilities of molybdenyl iodate $LiMoO_3(IO_3)$. The results were compared with the available experimental data and good agreement is found. The calculated linear optical properties reveal that there exists a considerable anisotropy favors an enhanced phase matching conditions necessary for observation of *SHG* and *OPO*. The linear optical properties show that $LiMoO_3(IO_3)$ possesses a positive birefringence and negative uniaxial anisotropy. It has been found that the molybdenyl iodate with $2D − Mo − O$ sheets capped by IO_3^- group is the main source of the *SHG* due to the electronic transition from the lone-pair electrons of oxygen atoms (O-2p) to Mo-4d and I-5p states and the presence of the alkali metals can give further strength to the *SHG*. We would like to mention that the arrangement of the dipole moments in MoO_6 octahedra and IO_3^- group are favorable for a large *SHG*. It is interesting to mentioned that our calculated value of the *SHG* for the dominant component agree well with the experimental value obtained by Chen's group, which is four times larger than that of the well know *KDP* (KH_2PO_4). Also we found that it is equal to one half of the experimental value of the well known $KTiOPO_4$ (*KTP*) single crystals. Further, the values of the microscopic first hyperpolarizability,

Fig. 2. (a) Calculated $\varepsilon_2^{xx}(\omega)$ (dark solid curve-black color online), $\varepsilon_2^{yy}(\omega)$ (light long dashed curve-red color online) and $\varepsilon_2^{zz}(\omega)$ (light dotted dashed curve-green color online) along with Calculated $\varepsilon_1^{xx}(\omega)$ (dark solid curve-blue color online), $\varepsilon_1^{yy}(\omega)$ (light dashed curve-brown color online) and $\varepsilon_1^{zz}(\omega)$ (light sold curve-violet color online) for $LiMoO_3(IO_3)$; (b) The optical transitions depicted on a generic band structure of $LiMoO_3(IO_3)$. For simplicity, we have labeled the optical transitions as A, B, and C. The transitions (A) are responsible for the structures for $\varepsilon_2^{xx}(\omega)$, $\varepsilon_2^{yy}(\omega)$ and $\varepsilon_2^{zz}(\omega)$ in the spectral range 0.0−5.0 eV; the transitions (B) 5.0−10.0 eV, and the transitions (C) 10.0−14.0 eV; (c) Calculated $R^{xx}(\omega)$ (dark solid curve-black color online), $R^{yy}(\omega)$ (light dashed curve-red color online), and $R^{zz}(\omega)$ (light dotted dashed curve-blue color online) for $LiMoO_3(IO_3)$; (d) Calculated $\sigma_2^{xx}(\omega)$ (dark solid curve-black color online), $\sigma_2^{yy}(\omega)$ (light dashed curve-red color online) and $\sigma_2^{zz}(\omega)$ (light dotted dashed curve-green color online) along with Calculated $\sigma_1^{xx}(\omega)$ (dark solid curve-blue color online), $\sigma_1^{yy}(\omega)$ (light dashed curve-red brown online) and $\sigma_1^{zz}(\omega)$ (light solid curve − violet color online) for $LiMoO_3(IO_3)$; (e) Calculated absorption coefficient $I^{xx}(\omega)$ (dark solid curve-back color online), $I^{yy}(\omega)$ (light dashed curve-red color online) and $I^{zz}(\omega)$ (light dotted dashed curve-blue color online) spectrum for $LiMoO_3(IO_3)$, the absorption coefficient in 10^4 cm^{-1}; (f) Calculated loss function $L^{xx}(\omega)$ (dark solid curve-back color online), $L^{yy}(\omega)$ (light dashed curve-red color online) and $L^{zz}(\omega)$ (light dotted dashed curve-blue color online) spectrum for $LiMoO_3(IO_3)$; (g) Calculated refractive indices $n^{xx}(\omega)$ (dark solid curve-black color online), $n^{yy}(\omega)$ (light dashed curve-red color online) and $n^{zz}(\omega)$ (light dotted dashed curve-blue color online) spectrum for $LiMoO_3(IO_3)$; (h) Calculated birefringence $\Delta n(\omega)$ for $LiMoO_3(IO_3)$. (For interpretation of the references to color in this figure legend, the reader is referred to the web version of this article.)

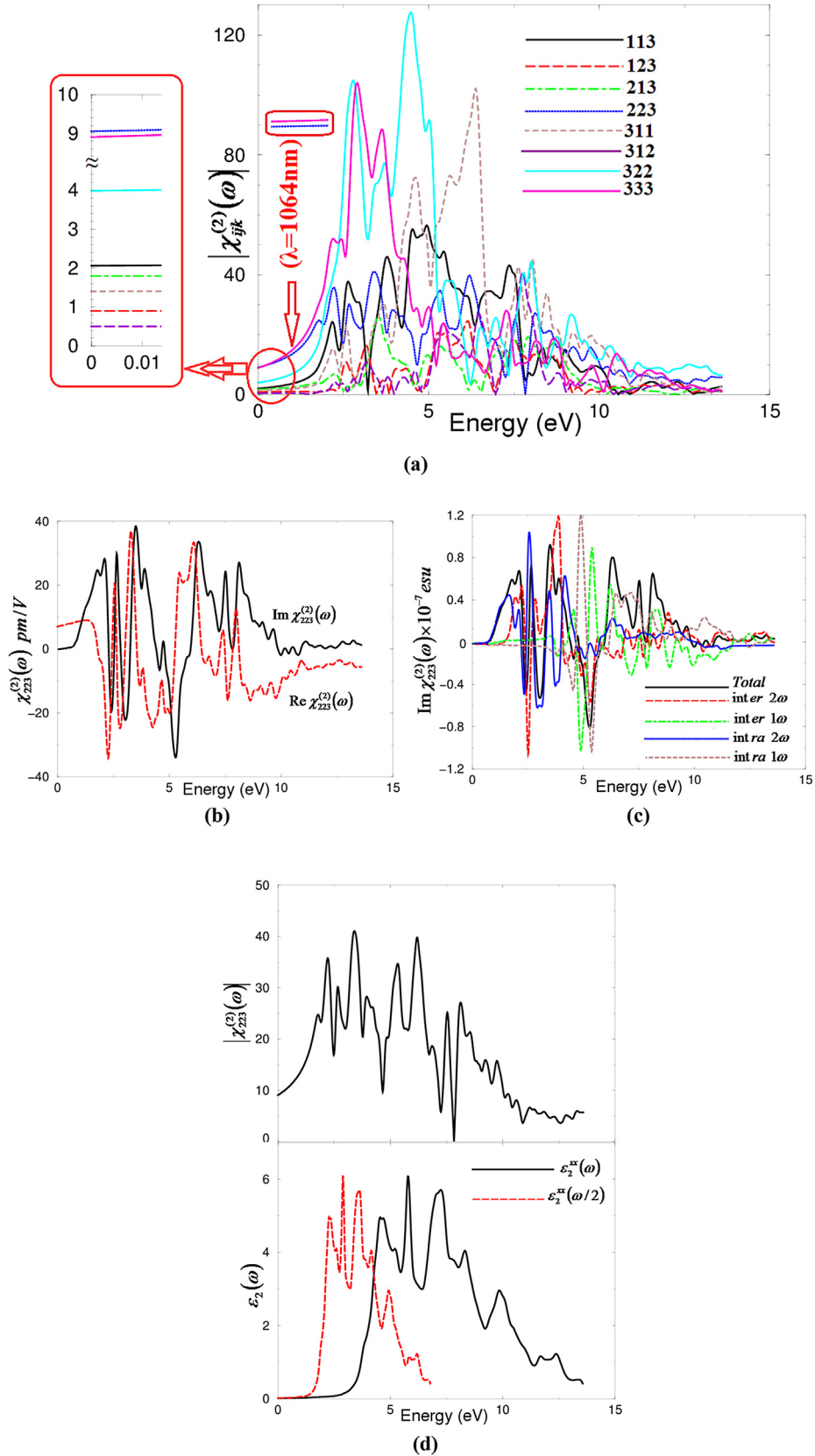**Fig. 3.** **(a)** Calculated $\left|\chi_{ijk}^{(2)}(\omega)\right|$ for the eight tensor components of LiMoO₃(IO₃); **(b)** Calculated Imaginary $\chi_{223}^{(2)}(\omega)$ (**dark solid curve-black color online**) and real $\chi_{223}^{(2)}(\omega)$ (light dashed curve-red color online) spectra of LiMoO₃(IO₃); **(c)** Calculated total Im$\chi_{223}^{(2)}(\omega)$ spectrum (**dark solid curve-black color online**) along with the intra (2ω)/(1ω) (light solid curve-blue color online)/(light dashed doted curve-cyan color online) and inter (2ω)/(1ω) (light long dashed curve-red color online)/(light doted curve-green color online)-band contributions of LiMoO₃(IO₃), here all Im$\chi_{222}^{(2)}(\omega)$ are multiplied by 10^{-7}, in esu units; **(d)** –***upper panel-*** Calculated $\left|\chi_{223}^{(2)}(\omega)\right|$ (dark solid curve-black color online); **-*lower panel-*** Calculated $\varepsilon_2^{xx}(\omega)$ (**dark solid curve-black color online**); Calculated $\varepsilon_2^{xx}(\omega/2)$ (**dark dashed curve-red color online**) of LiMoO₃(IO₃). (For interpretation of the references to color in this figure legend, the reader is referred to the web version of this article.)

Table 2
Calculated $\left|\chi_{ijk}^{(2)}(\omega)\right|$ and β_{ijk} of LiMoO$_3$(IO$_3$), in pm/V at static limit and at $\lambda = 1064$ nm, in comparison with the experimental value of the well known KTiOPO$_4$ (KTP) single crystals which exhibits a SHG value of about 16.9 [34], 13.7 [35], 15.4 ± 0.2 [36], 14.6 ± 1.0 [37], 17.4 ± 1.7 [38], 16.9 ± 3.3 [39], 16.9 ± 1.7 [40], 10.6 ± 7.5 [41], 16.75 [42] and 16.65 [42] at $\lambda = 1064$. Where 1 pm/V = 2.387×10^{-9} esu.

Tensor components	$\chi_{ijk}^{(2)}(0)$	Theory $d_{ijk} = 0.5\chi_{ijk}^{(2)}(\omega)$	$\chi_{ijk}^{(2)}(\omega)$ at $\lambda = 1064$	Theory $d_{ijk} = 0.5\chi_{ijk}^{(2)}(\omega)$
$\left|\chi_{113}^{(2)}(\omega)\right|$	2.022	$d_{15} = 1.011$	4.232	$d_{15} = 2.116$
$\left|\chi_{123}^{(2)}(\omega)\right|$	0.893	$d_{14} = 0.446$	1.055	$d_{14} = 0.527$
$\left|\chi_{213}^{(2)}(\omega)\right|$	1.787	$d_{25} = 0.893$	2.891	$d_{25} = 1.445$
$\left|\chi_{223}^{(2)}(\omega)\right|$	**9.059**	$\mathbf{d_{24} = 4.529}$	15.105	$d_{24} = 7.552$
$\left|\chi_{311}^{(2)}(\omega)\right|$	1.410	$d_{31} = 0.705$	2.185	$d_{31} = 1.092$
$\left|\chi_{312}^{(2)}(\omega)\right|$	0.516	$d_{36} = 0.258$	0.561	$d_{36} = 0.280$
$\left|\chi_{322}^{(2)}(\omega)\right|$	4.046	$d_{32} = 2.023$	8.257	$d_{32} = 4.128$
$\left|\chi_{333}^{(2)}(\omega)\right|$	8.918	$d_{33} = 4.459$	**16.941**	$\mathbf{d_{33} = 8.470}$
β_{223}	$\mathbf{2.432 \times 10^{-30}}$		4.063×10^{-30} at ($\lambda = 1064$ nm)	
β_{333}	2.386×10^{-30}		$\mathbf{4.458 \times 10^{-30}}$ **at ($\lambda = 1064$ nm)**	

β_{ijk} was obtained for the dominant components at static limit and at $\lambda = 1064$ nm. It has been found that the value of β_{223} about 2.432×10^{-30} (4.063×10^{-30}) while for β_{333} is about 2.386×10^{-30} (4.458×10^{-30}) at the static limit ($\lambda = 1064$ nm).

Appendix A. Supplementary data

Supplementary data related to this article can be found at http://dx.doi.org/10.1016/j.jallcom.2015.11.076.

References

[1] P. Becker, Adv. Mater. Weinheim Ger. 10 (1998) 979.
[2] J. Barbier, N. Penin, A. Denoyer, L.M.D. Cranswick, Solid State Sci. 7 (2005) 1055.
[3] J. Barbier, N. Penin, L.M. Cranswick, Chem. Mater 17 (2005) 3130.
[4] J. Barbier, L.M.D. Cranswick, J. Solid State Chem. 179 (2006) 3958.
[5] A.H. Reshak, S. Auluck, I.V. Kityk, Curr. Opin. Solid State Mater. Sci. 12 (2009) 14–18.
[6] A.H. Reshak, D. Stys, S. Auluck, I.V. Kityk, PCCP 12 (2010) 2975–2980.
[7] A.H. Reshak, H. Kamarudin, S. Auluck, B. Minofar, I.V. Kityk, Appl. Phys. Lett. 98 (2011), 201903–201911-201903-3.
[8] A. Wojciechowski, I.V. Kityk, A.H. Reshak, R. Miedzinski, K. Ozga, J. Berdowski, Z. Tylczyński, Mater. Lett. 64 (2010) 1957–1959.
[9] A.H. Reshak, D. Stys, S. Auluck, I.V. Kityk, H. Kamarudin, J. Mater Chem. Phys. 130 (2011) 458–465.
[10] A.H. Reshak, H. Kamarudin, S. Auluck, J. Phys. Chem. B 116 (2012) 4677–4683.
[11] V. Kapustianyk, B. Turko, A. Kostruba, Z. Sofiani, B. Derkowska, S. Dabos-Seignon, B. Barwinski, Yu Eliyashevskyi, B. Sahraoui, Opt. Commun. 269 (2007) 346–350.
[12] S. Zongo, A.P. Kerasidou, B.T. Sone, A. Diallo, P. Mthunzi, K. Iliopoulos, M. Nkosi, M. Maaza, B. Sahraoui, Appl. Surf. Sci. 340 (2015) 72–77.
[13] Ts Kolev, I.V. Kityk, J. Ebothe, B. Sahraoui, Chem. Phys. Lett. 443 (2007) 309–312.
[14] Hasnaa El Ouazzani, Konstantinos Iliopoulos, Mindaugas Pranaitis, Oksana Krupka, Vitaliy Smokal, Aleksey Kolendo, Bouchta Sahraoui, J. Phys. Chem. B 115 (9) (2011) 1944–1949.
[15] M. Derbazi, A. Migalska-Zalas, G. Goldowski, I.V. Kityk, H. El Ouazzani, J. Ebothé, B. Sahraoui, Opt. Mater. 34 (2012) 1261–1266.
[16] S. Abed, H. Bougharraf, K. Bouchouit, Z. Sofiani, B. Derkowska-Zielinska, M.S. Aida, B. Sahraoui, Superlatt. Microstruct. 85 (2015) 370–378.
[17] O.P. Kwon, M. Jazbinsek, Jung-In Seo, Eun-Young Choi, Hoseop Yun, F.D.J. Brunner, Yoon Sup Lee, P. Günter, J. Chem. Phys. 130 (2009) 134708–134714.
[18] J. Zyss, J.L. Oudar, Phys. Rev. A 26 (1982) 2028–2048.
[19] Xuean Chen, Li Zhang, Xinan Chang, Haiping Xue, Hegui Zang, Weiqiang Xiao, Xuemei Song, Hui Yan, J. Alloys Compd. 428 (2007) 54–58.
[20] Chun-Li Hu, Jiang-Gao Mao, J. Phys. Condens. Matter. 22 (2010) 155801.
[21] A.H. Reshak, S. Auluck, RSC Adv. 4 (2014) 37411.
[22] A.H. Reshak, RSC Adv. 4 (2014) 39565.
[23] M. Jamal, N. Kamali Sarvestani, A. Yazdani, A.H. Reshak, RSC Adv. 4 (2014) 57903.
[24] A.H. Reshak, RSC Adv. 4 (2014) 63137.
[25] J.P. Perdew, S. Burke, M. Ernzerhof, Phys. Rev. Lett. 77 (1996) 3865.
[26] P. Blaha, K. Schwarz, G.K.H. Madsen, D. Kvasnicka, J. Luitz, WIEN2k, an Augmented Plane Wave Plus Local Orbitals Program for Calculating Crystal Properties, Vienna University of Technology, Austria, 2001.
[27] F. Tran, P. Blaha Phys, Rev. Lett. 102 (2009) 226401.
[28] H. Tributsch, Z. Naturforsch. A 32A (1977) 972.
[29] D.R. Penn, Phys. Rev. B 128 (1962) 2093.
[30] S. Sharma, J.K. Dewhurst, C. Ambrosch-Draxl, Phys. Rev. B 67 (2003) 165332.
[31] A.H. Reshak, Indian Institute of Technology-Rookee, India (Ph.D. thesis), 2005.
[32] A.H. Reshak, J. Chem. Phys. 125 (014708) (2006).
[33] A.H. Reshak, J. Chem. Phys. 124 (014707) (2006).
[34] K. Zhang, X. Wang, Chin. Sci. Bull. 46 (2001) 2028–2036.
[35] http://www.castech-us.com/casktp.htm.
[36] M.V. Pack, D.J. Armstrong, A.V. Smith, Appl. Opt. 43 (2004) 3319.
[37] T. Shoji, A. Kondo, M. Kitamoto, Shirane, R. Ito, J. Opt. Soc. Am. B 14 (1997) 2268.
[38] A. Anema, T. Rasing, Appl. Opt. 36 (1997) 5902.
[39] L.K. Cheng, L.T. Cheng, J. Galperin, P.A.M. Hotsenpiller, J.D. Bierlein, J. Cryst. Growth 137 (1994) 107.
[40] H. Vanherzeele, J.D. Bierlein, Opt. Lett. 17 (1992) 982.
[41] B. Boulanger, J.P. Feve, G. Marnier, B. Menaert, Pure Appl. Opt. 7 (1998) 239.
[42] A.H. Reshak, I.V. Kityk, S. Auluck, J. Phys. Chem. B 114 (2010) 16705–16712.
[43] A.H. Reshak, D. Stys, S. Auluck, I.V. Kityk, J. Phys. Chem. B 114 (2010) 1815–1821.
[44] X. Chen, L. Zhang, X. Chang, H. Xue, H. Zang, W. Xiao, X. Song, H. Yan, J. Alloys Compd. 428 (2007) 54.
[45] R.E. Sykora, K.M. Ok, P.S. Halasyamani, T.E. Albrecht-Schmitt, J. Am. Chem. Soc. 124 (2002) 1951.
[46] (a) N. Ye, Q. Chen, B. Wu, C. Chen, J. Appl. Phys. 84 (1998) 555–558;
(b) B. Wu, D. Tang, N. Ye, C. Chen, Opt. Mater. 5 (1996) 105–109;
(c) Chuangtian. W. Yebin, W. Baichang, W. Keche, Z. Wenlun, Y. Linhua, Nature 373 (1995) 322–324.
[47] A.H. Reshak, S. Auluck, D. Stys, I.V. Kityk, H. Kamarudin, J. Berdowskie, Z. Tylczynski, J. Mater. Chem. 21 (2011) 17219.
[48] A.H. Reshak, V. Kityk, S. Auluck, J. Phys. Chem. B 114 (2010) 16705–16712.
[49] R.Y. Boyd, Principles of Nonlinear Optics, Academic Press, NY, 1982, p. 420.
[50] R.W. Boyd, Nonlinear Optics, third ed., Academic Press is an Imprint of Elsevier, 2008, ISBN 978-0-12-369470-6.